

## Study of the bubble motion in a compound couette-Poiseuille flow: Effect of the pressure gradient

Morteza Bayareh<sup>1</sup>, Amireh Nourbakhsh<sup>2\*</sup>

<sup>1</sup> Department of Mechanical Engineering, Shahrekord University, Shahrekord, Iran

<sup>2</sup> Department of Engineering, Bu-Ali Sina University, Hamedan, Iran

Corresponding Author Email: [nourbakhsh@basu.ac.ir](mailto:nourbakhsh@basu.ac.ir)

[https://doi.org/10.18280/ama\\_a.550102](https://doi.org/10.18280/ama_a.550102)

**Received:** 31 December 2017

**Accepted:** 14 March 2018

### **Keywords:**

*migration, finite-difference/front-tracking method, pressure gradient, combined couette-poiseuille flow*

### **ABSTRACT**

In the present study, the numerical simulation of lateral migration of a three-dimensional deformable bubble in a compound laminar Couette and Poiseuille flow is studied at finite Reynolds numbers. The Navier-Stokes equations are solved for incompressible fluids using a finite-difference method on a regular, fixed, and staggered grid. Interface is tracked explicitly by connecting marker points through a front-tracking method on a triangular moving grid. The effects of surface tension are also accounted for by adding an appropriate source term to the governing equations. The results show that a bubble, regardless of its original position, will be fixed in an equilibrium position between the wall and the centerline of channel. It is observed that by increase of the bubble radius, the bubble migrates to an equilibrium position closer to the centerline. Negative pressure gradient causes that the deformation of bubble increases, so it reaches a steady-state position closer to the center line.

## 1. INTRODUCTION

The suspension of particles, such as drop, bubble and rigid particle through channels and pipes is subject of many theoretical, numerical and experimental investigations. Bubble industrial applications include power generation units, such as oil pipelines, steam generators, and cooling systems. The idea of using gas liquid to lubricate the motion of floating objects backs to 1880, but the first recorded applied research in this field was conducted by McCormick and Bhattacharyya in 1973[1]. In this study, they electrolyzed water, followed by releasing of hydrogen bubbles around floating hydrofoil in water. The results showed that with increasing flow rate and increasing the amount of released hydrogens, the model velocity compared to normal mode. This happened due to changes in viscosity of the fluid near the wall and distortion the viscous layer by bubbles. One example of its application in underwater industries is reduced surface tensions, followed by higher velocity, lower power and energy. One of the proposed methods is using second phase, in a way the considered underwater structure that can be submarine or torpedoes moves on a cushion of air by creating bubbles in the boundary layer. Second phase can be created through various methods. The second phase can be water vapor, different gases or fluid different from the first fluid. Bubbles are created through gases soluble in water, as result of chemical reactions or as result of cavitation in heavy and strong flows. The other applications of bubble in chemical engineering are gas-liquid column reactors and gas-liquid-solid reactors, which are widely used in industrial operations [2].

The migration of dilute suspensions of neutrally buoyant solid particles in pipe flow was first shown by Segre and Silberberg [3, 4] at finite Reynolds numbers. They found that the particles move to an equilibrium lateral position about halfway between the centerline and the wall. An experimental

study of the migration of suspensions of particles in Poiseuille flow in a wide range of Reynolds numbers was performed by Matas et al. [5] They extended the results of Segre and Silberberg and showed that the tubular pinch effect in which particles accumulate is moved toward the wall as the Reynolds number increases.

Several numerical methods have been used in the past to study the behavior of multiphase systems in the presence of solid boundaries. These numerical methods included volume-of-fluid, Lattice-Boltzmann, finite difference, finite element, boundary-integral and Level-set methods. For example, Griggs, Zinchenko & Davis [6] used a boundary-integral algorithm to investigate the creeping motion of a three-dimensional deformable drop or bubble in the vicinity of an inclined wall. They showed that the steady velocities of drops (made dimensionless by the settling velocity of an isolated spherical drop) increase with increasing Bond number for intermediate-to-large inclination angles (i.e.  $45^\circ \leq \theta \leq 75^\circ$ ). However, the steady drop velocity is not always an increasing function of Bond number for viscous drops at smaller inclination angles. Results of dynamic simulations of the pressure-driven flow of a two-dimensional suspension in a channel confined between two parallel walls were simulated by Li and Pozrikidis[7]. They studied the effect of the capillary number, viscosity ratio and the effective viscosity of suspension. A three-dimensional study of the motion of a drop in plane Poiseuille flow at finite Reynolds numbers was conducted by Nourbakhsh and Mortazavi [8]. They showed that the drop moves to an equilibrium lateral position about halfway between the wall and the centerline (the Segre-Silberberg effect). As the Reynolds number increases or capillary number or viscosity ratio decreases, the equilibrium position moves closer to the wall. The deformation of neutrally buoyant drops and bubbles moving through straight tubes and constrictions in plane Poiseuille flow has been simulated by

Tsai and Miksis [9]. They indicated that for small values of capillary number a steady-state solution can be found, but the drop deformation increases with increasing capillary number due to the increase in viscous stresses along the interface. The flow of drops suspended on an inclined surface, were studied by Mortazavi and Tafreshi [10]. The effect of the Reynolds number, the capillary number and density ratio on the distribution of drops and the fluctuation energy across the channel were investigated. They found that drops tend to stay away from the channel floor, which is consistent with the behavior observed in the granular flow regime. They also indicated that drops that are less deformable will stay further away from the channel floor. Also, drops appear at a larger distance from the floor as the Reynolds number increases. Bayareh and Mortazavi [11] performed a three-dimensional study of suspension of drops in simple shear flow at finite Reynolds numbers. Results were obtained using a finite difference/front tracking method in a periodic domain. They studied the effects of the Reynolds number and the capillary number at two volume fractions: 0.195 and 0.34 and observed that suspensions of deformable drops exhibit a shear-thinning behavior. They also found that the effective viscosity, the first and the second normal stress differences oscillate around a mean value in all cases. The first normal stress difference increases with the capillary number, the Reynolds number and the volume fraction. Results also showed that drops deform more and orient more in the flow direction as the capillary number or the volume fraction is increased. The collision of two equal-size drops in an immiscible phase undergoing a shear flow was simulated by Bayareh and Mortazavi [12] over a range of viscosity ratios and different geometries. The distance between drop centres along the velocity gradient direction (z) was measured as a function of time. They found that  $\Delta z$  increases after collision and reaches a new steady-state value after separation. The values of  $\Delta z$ , during the interaction, increases with increasing initial offset. Their results show that the time of approaching of drops at low initial offset is greater than the other cases, but the maximum deformation is the same for equal drop sizes. They showed that deformation decreases with decreasing the size of drops. Numerical simulation of sedimenting deformable drops inside a vertical channel has been performed by Amiri and Mortazavi [13]. They illustrated that the wall repulsion is the main mechanism of the lateral migration of the drop, and drop migrates toward the channel axis. When the Reynolds number is relatively low, two different lateral migration regimes were observed: migration with monotonic approach and migration with damped oscillations. They indicated that when the Bond number increases, the oscillations of drop around the centerline of channel are stronger and drop reaches the channel centerline in a larger period.

While the numerous studies mentioned above constitute considerable progress towards understanding the motion of drops and bubbles in channels in a Couette or a Poiseuille flow, some important unresolved issues and computational challenges still remain. In particular, there is a need for a three-dimensional systematic assessment of a bubble in both flow (Couette and Poiseuille flow) at finite Reynolds numbers. Thus, the main objective of the current effort is to employ the finite difference/front tracking method to a three-dimensional neutrally buoyant bubble between two parallel plates in the compound Couette and Poiseuille flow.

## 2. GOVERNING EQUATIONS AND NUMERICAL METHOD

The equations govern the motion of unsteady, viscous, incompressible, and immiscible two-fluid systems are the Navier-Stokes equations [8]:

$$\frac{\partial \rho \mathbf{u}}{\partial t} + \nabla \cdot \rho \mathbf{u} \mathbf{u} = -\nabla P + \nabla \cdot \mu (\nabla \mathbf{u} + \nabla \mathbf{u}^T) + \sigma \int \kappa \delta^\beta (\mathbf{x} - \mathbf{x}') d_s \quad (1)$$

where,  $\mathbf{u}$  is the velocity,  $P$  is the pressure, and  $\rho$  and  $\mu$  are the discontinuous density and viscosity fields, respectively.  $\sigma$  is the surface tension coefficient and  $\mathbf{f}$  is a body force. Surface forces are added at the interface. The term  $\delta^\beta$  is a two- or three-dimensional  $\delta$  function constructed by repeated multiplication of one-dimensional  $\delta$  functions. The dimension is denoted by  $\beta = 2$  or  $3$ ,  $\kappa$  is the curvature for two-dimensional flow and twice the mean curvature for three-dimensional flows,  $\mathbf{n}$  is a unit vector normal to the front,  $\mathbf{x}$  is the point at which the equation is evaluated,  $\mathbf{x}'$  is a Lagrangian representation of the interface.

This equation is solved by a second-order projection method using centred differences on a fixed regular staggered grid. Both the bubble and the ambient fluid are taken to be incompressible, so the velocity field is divergence free [15]:

$$\nabla \cdot \mathbf{u} = 0 \quad (2)$$

Equation (3), when combined with the momentum equation, leads to a non-separable elliptic equation for the pressure. If the density is constant, the elliptic pressure equation is solved by fast Poisson solver (FISHPACK), but when the density of the bubble is different from the suspending fluid, the equation is solved by a multigrid method [18].

Equations of state for the density and the viscosity are:

$$\frac{D\rho}{Dt} = 0, \quad \frac{D\mu}{Dt} = 0 \quad (3)$$

where,  $D/Dt$  is the material derivative, and equation (3) simply states that the density and the viscosity of each fluid remain constant.

The governing dimensionless numbers are the ratio of the viscosity of the bubble fluid to the suspending medium  $\lambda = \mu_i / \mu_o$ , the density ratio  $\alpha = \rho_i / \rho_o$ , and the ratio of the radius of the bubble to the height of the channel  $\zeta = a / H$ . The viscosity and density of the bubble liquid are denoted by  $\mu_i$  and  $\rho_i$ , respectively, and the suspending fluid has viscosity  $\mu_o$  and density  $\rho_o$ . The bulk Reynolds number is defined in terms of the undisturbed channel centerline velocity ( $U_c$ ) and the channel height, as  $\text{Re}_b = \rho_o U_c H / \mu_o$ . A Reynolds number based on the centerline velocity and the bubble diameter ( $d$ ) is defined by  $\text{Re}_d = \rho_o U_c d / \mu_o$ . A particle Reynolds number can be defined as  $\text{Re}_p = \rho U_c a^2 / \mu H$ . The capillary number,  $Ca = U_c \mu_o / \sigma$  describes the ratio of the viscous stress to the interfacial tension. Dimensionless time is defined by  $t^* = t U_c / H$ .

## 2.1. Numerical method

One of the most important problems of computational fluid mechanics is flows with interfaces. Different numerical methods are used and developed for simulating these flows. These methods can be divided into two groups, depending on the type of grids used: moving grid and fixed grid. Two main approaches of fixed-grid methods are the volume-of-fluid (VOF) and level-set methods. The volume-of-fluid method uses a marker function. The main difficulty in using VOF method is surface tension term. The level-set method defines the interface by a function  $\phi$ . But this approach has some difficulties in preserving the mass conservation. Another method presented in this paper is front-tracking method which improved the disadvantages of the previous methods. This approach has been described in detail by Unverdi & Tryggvason [15,16] and only a brief outline is given here. The present simulations are based on an improved implementation of the front-tracking method at finite Reynolds numbers that include convective terms. The numerical technique is based on a direct discretization of the Navier-Stokes equation.

## 2.2. Problem setup

The geometry of the problem is shown in Fig. 1. The motion of a bubble is studied in a channel that is bounded by two flat plates in  $z$ -direction. The height and length of the channel are  $H$ . The boundary condition on the plates is the no-slip condition. The domain is periodic in the  $x$ - and  $y$ -directions. Normal stresses show jump across the interface by surface tension and tangential stresses are continuous on the surface of the drop. To decrease the computational time, the depth of the channel in the  $y$ -direction is taken to be  $0.5 H$ . In addition, the previous simulations demonstrated the variation in  $y$ -direction is negligible [8]. In the absence of the bubble, the undisturbed flow is driven by a constant pressure gradient [8-14]):

$$\nabla p = \nabla p_o + \nabla p' \quad (4)$$

where  $\nabla p_o$  is the externally specified pressure gradient and  $\nabla p'$  is the perturbation pressure gradient to be computed as part of the solution. Gravity is neglected and buoyancy effects are negligible.

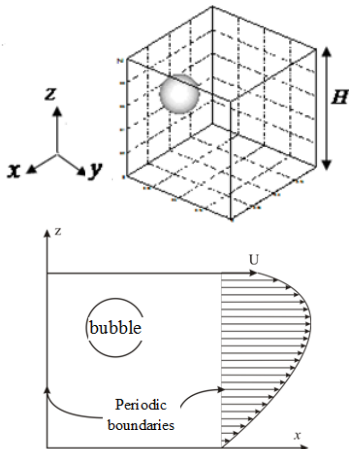


**Figure 1.** The geometry for the simulation of a bubble in a channel

## 2.3. Resolution test

In this section, the grid study is conducted to evaluate the independence of results from the grid resolution. Fig. 2 shows lateral position of a bubble versus dimensionless time at four different grid resolutions of  $32 \times 16 \times 32$ ,  $48 \times 24 \times 48$ ,  $64 \times 32 \times 64$  and  $96 \times 48 \times 96$ . Flow conditions are as follows:  $Re_d = 10$ ,  $Ca = 0.9$ ,  $\alpha = \lambda = 0.8$  and  $\xi = 0.125$ . The computational domain is assumed to be  $1 \times 0.5 \times 1$ .

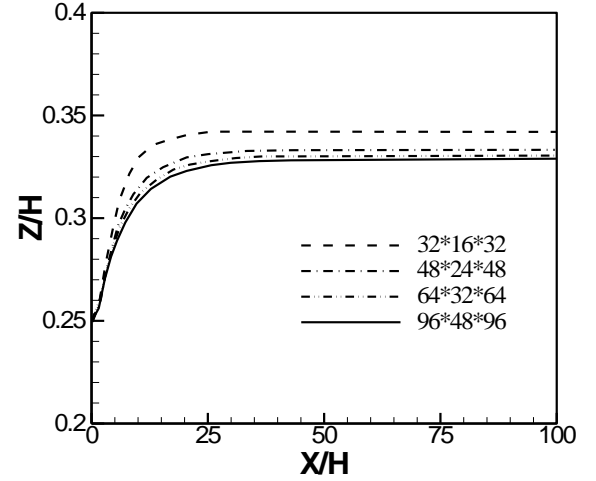


**Figure 2.** The lateral position versus the axial location of a bubble at four different grid resolutions.

Since the difference between the results predicted using  $64 \times 32 \times 64$  and  $96 \times 48 \times 96$  grid points is smaller than the difference between the results predicted using  $32 \times 16 \times 32$  and  $64 \times 32 \times 64$  grids, the  $64 \times 32 \times 64$  resolution is used for all simulations performed in this study to achieve a reasonable time. The streamlines for a cross-section at  $y = 0.25$  at steady state are shown for a bubble at  $Ca = 0.3$  with  $64 \times 32 \times 64$  grid points in Fig. 3. Flow parameters are  $Re_d = 10$ ,  $\alpha = \lambda = 0.8$  and  $\xi = 0.125$ . The figure shows fluid circulation inside the bubble. The circulation is a difference between the rigid and deformable particles. The time step is  $10^{-5}$  for all simulations. In addition, the convergence criterion for the iterative solver is a maximum change of  $10^{-6}$  in the normalized drop trajectory.

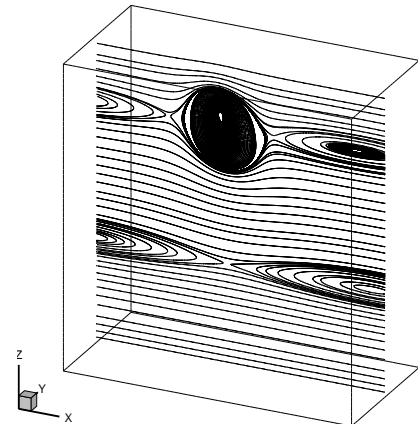


**Figure 3.** Streamlines in the middle section in the  $y$ -direction for a bubble with capillary number  $Ca = 0.3$ .

### 3. RESULTS AND DISCUSSION

The flow through the gap between the bubble and the wall leads to a repulsive lubrication force called ‘geometric blocking’ that pushes the drop away from the wall [19]. The negative slip velocity and the curvature of the velocity profile in Poiseuille flow, generate a force that drives the drop away from the center of the channel. So, these two forces move the drop to an equilibrium position about halfway between the centerline and the wall (the Segre-Silberberg effect).

A three-dimensional study of the motion of a bubble in the compound couette-poiseuille flow that is presented in this section are compared with Poiseuille flow presented in numerical reports so that their appellation and differentiate with numerical simulations performed in this study to be determined. For this purpose, results are compared with numerical simulations obtained by Feng et al. [19-20]. Figure 4 shows the lateral positions versus the dimensionless time for a bubble that is released at different initial positions. As could be seen in Fig. 4, the equilibrium distance from upper wall is  $z_{eq}/H= 0.224$  and it is  $z_{eq}/H= 0.288$  from lower wall. The important result that can be derived by conducting these simulations is that Segre-Silberberg effect can be seen also in combined Couette and Poiseuille flow. However, in the considered flow, equilibrium position is slightly different from the simulations conducted by Feng et al. [19-20] in Poiseuille flow. The cause of this difference can be found in velocity profile curvature. Since the velocity profile in a combined flow of Couette and Poiseuille tends towards mid-upper channel, the effect of velocity profile curvature is stronger than Poiseuille flow and the equilibrium position will be at a closer distance to the upper wall. Similarly, in mid-lower part of channel, as the effect of velocity profile is lower than Poiseuille flow, equilibrium position will be close to the center line.

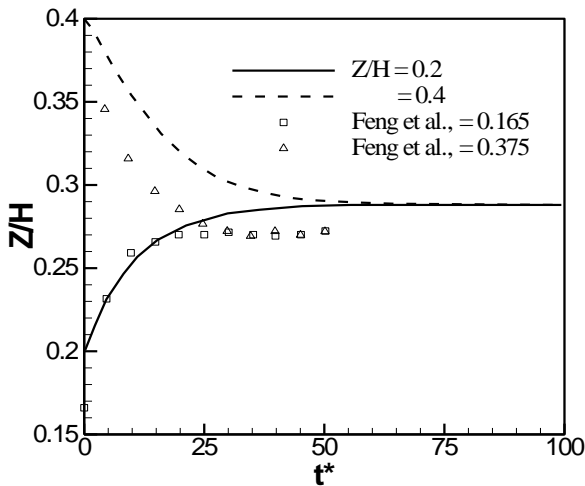


**Figure 4.** Comparison of the simulated Segre-Silberberg effect with the simulation of Feng et al. [19-20]

#### 3.1 Effect of the bubble size

In Fig. 5, the lateral position of the bubble is plotted versus the axial position for three bubbles with different sizes. Flow parameters include:  $Re_d = 10$ ,  $Ca = 0.2$  and  $\xi = 0.18$ ,  $\xi = 0.2$ ,  $\xi = 0.22$ . Mortazavi and Triggvason [14] demonstrated that for large droplets, periodic length can have a significant impact, but this effect is insignificant for the small droplets. As a

result, in order to reduce the impacts of periodic boundary conditions, the length of computational domain has been doubled. The size of the computational domain is  $2 \times 1 \times 2$  and the grid resolution is  $96 \times 48 \times 96$  in the x-, y- and z-directions, respectively.

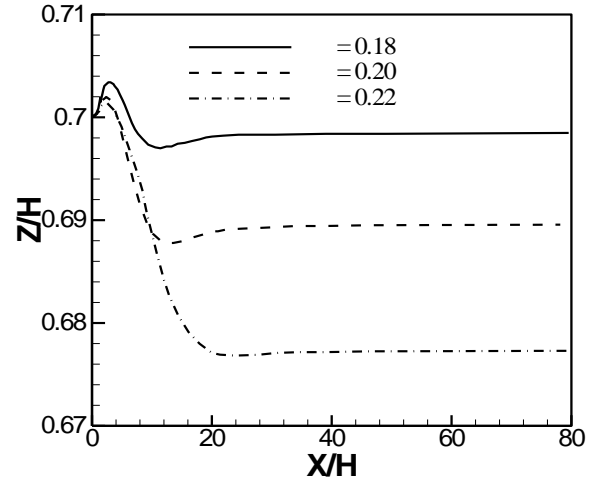


**Figure 5.** The lateral position versus the axial position at three different bubble sizes

It is observed that with increasing the radius of the bubble, after a transition period, which is associated with a fluctuation, the centroid of the bubble moves away from the upper wall. This is due to the fact that a larger lubrication force results for the larger bubble. This force moves the bubble further away from the wall. Similar phenomenon was observed by Mortazavi and Tryggvason [14] and Nourbakhsh and Mortazavi [8]. The bubbles initially migrate towards the upper wall, and then move to an equilibrium lateral position. The reason behind this cause is explained. The flow through the gap between the bubble and the wall leads to a repulsive lubrication force called ‘geometric blocking’ by Feng et al. [19], that pushes the bubble away from the wall. The negative slip velocity and the curvature of the velocity profile in Poiseuille flow, generate a force that drives the bubble away from the center of the channel. So, these two forces move the bubble to an equilibrium position about halfway between the centerline and the wall (the Segre-Silberberg effect). In Fig. 6, the migration rate or lateral velocity of bubble is shown against dimensionless time. It is observed that in the transient period, the bubble firstly will move toward the upper wall with a positive rate and then will move quickly toward the bottom wall with a negative rate, and, after being fixed in a state of equilibrium, its migration rate will also be zero which agrees with our ideas of this phenomenon.

To describe the shape of the bubble, the deformation parameter  $D = (L-b)/(L+b)$  is considered, where  $L$  and  $b$  are, respectively, the maximum and minimum bubble dimensions (Taylor [21]). The deformation of the bubble is plotted versus dimensionless time in Fig. 7. The deformation increases with increasing the radius of the bubble. As the area of the bubble increases, the effect of the upper plate becomes increasingly more important because more fluid is pushed through a smaller gap, requiring a greater local pressure gradient and increasing deformation. Schelizer & Bonnecaze [22], Doddi & Bagchi [23] and Martinez & Udell [24] showed

that as the size of the droplet increases, the deformation of the drop increases as well.

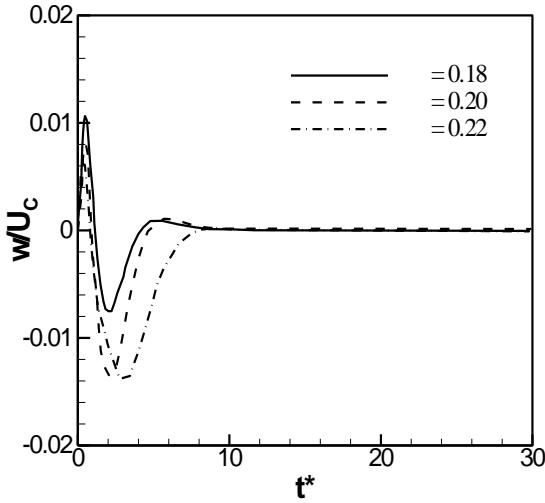


**Figure 6.** Lateral velocity versus dimensionless time at three different bubble sizes

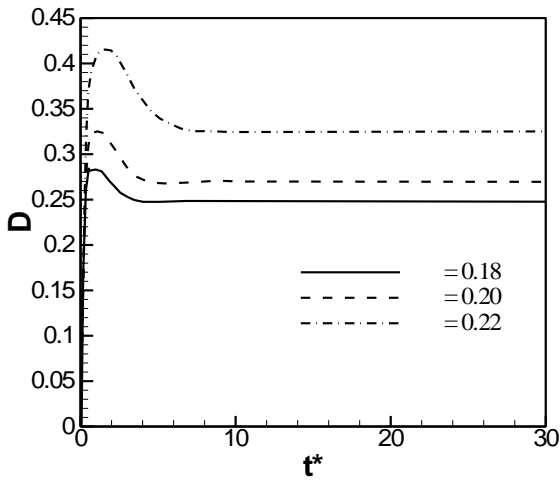


**Figure 7.** Bubble deformation versus dimensionless time at three different bubble sizes

### 3.2 Effect of pressure gradient

In the Couette flow, the driver factor of the flow is velocity of the upper wall; also in the Poiseuille flow, the driver factor of the flow is the pressure gradient, but in the compound flow both factors can be influential. Since in the Poiseuille flow, velocity profile is symmetric to the center line of the channel, applying the symmetry of pressure gradient only in the axial direction of immigration can be effective, but in the compound flow, because of the mobility of the upper wall, the velocity profile has not been symmetric. In this section, the impact of positive or negative pressure gradient on the bubble migration is considered.

For this purpose, two simulations with dimensionless pressure gradient  $P = 7.8728$  and  $P = -7.8728$  have been done. Here, the pressure gradient is defined as  $P = \left(-\frac{dp}{dx}\right) \frac{h^2}{2\mu U}$ . The flow conditions are  $Re_d = 10$ ,  $\alpha = \lambda = 0.8$ . In Fig. 8, the lateral position based on dimensionless time has been observed. As it stands, the bubble with the negative pressure

gradient is in a state of equilibrium closer to the center line. The reason is that in the flow with reverse pressure gradient, the shear rate is more and the bubble deforms more; thus the lubrication force between the bubble and the wall, which is known as ‘geometric blocking’ by Feng et al. [19, 20], will get more and pushes the bubble to a state of equilibrium farther to the wall.

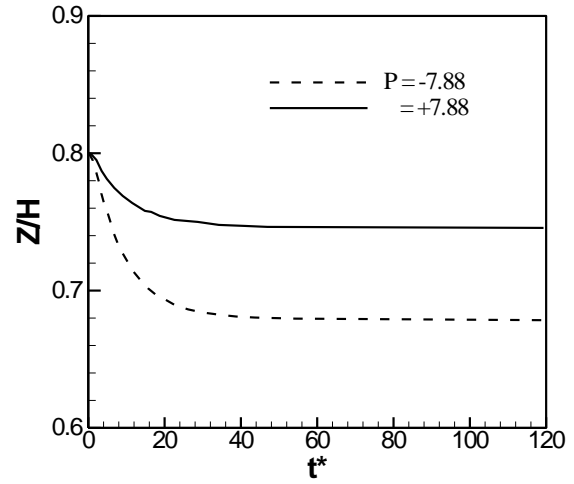


**Figure 8.** Effect of the pressure gradient on the lateral migration of a bubble

In Fig. 9, the quantity of Taylor deformation based on dimensionless time is shown; as it is seen, rate of deformation in adverse pressure gradient is greater than the positive pressure gradient which is consistent with our imaginations about this phenomenon.

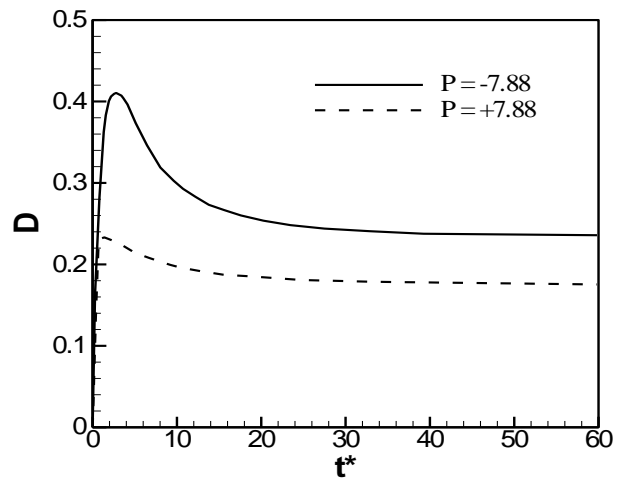


**Figure 9.** Effect of the pressure gradient on Taylor deformation

The lateral velocity of the bubble is plotted versus time in Fig. 10. As it is seen, during the transition period, the lateral velocity has a negative value. Lateral velocity initially starts from zero and after passing the transition period, when the bubble reaches an equilibrium lateral position about halfway between the centerline and the wall, becomes zero. Also the adverse pressure gradient has a greater lateral velocity than the positive pressure gradient.

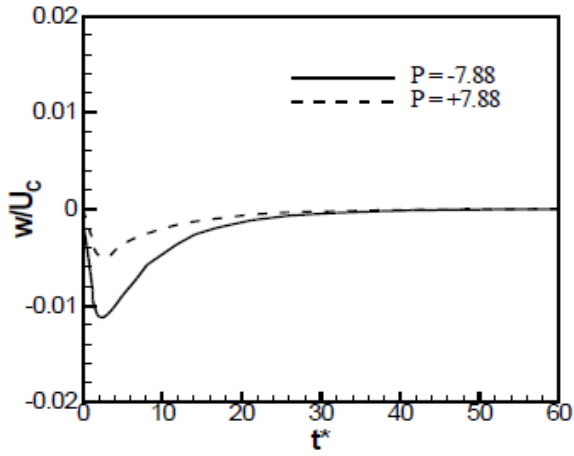


**Figure 10.** Effect of the pressure gradient on the lateral velocity

In Fig. 11, the slip velocity has been plotted based on dimensionless time.

As is clear in Figure 12 (a) about the flow with positive pressure gradient, when the bubble is in a stable equilibrium position, velocity profile in the presence of bubble is little further than the unperturbed velocity profile; also similar result can be achieved for the flow with negative pressure gradient (Figure 12 (b)).

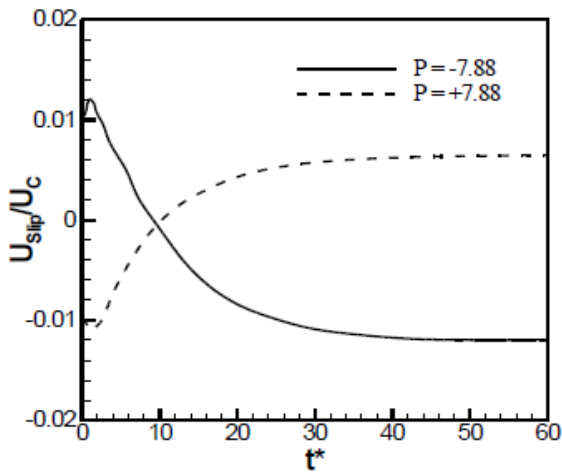
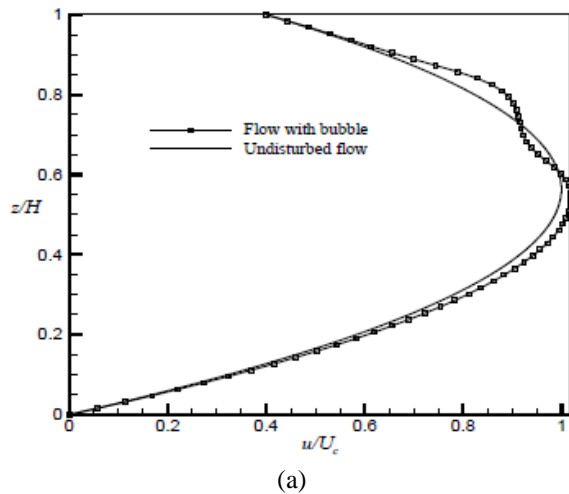
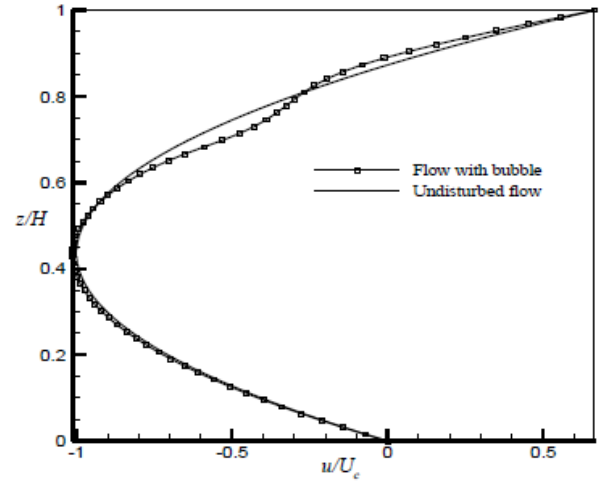


**Figure 11.** Effect of the pressure gradient on the slip velocity



(a)



(b)

**Figure 12.** The velocity profile for the unperturbed flow and flow with bubble a) positive pressure gradient and b) negative pressure gradient

The streamlines at steady state are shown for bubbles with positive and adverse pressure gradient in Figs. 13 and 14. As it is clear, the flow patterns are similar; the only difference is in the angle of the main axis of bubble with the wall of the channel.

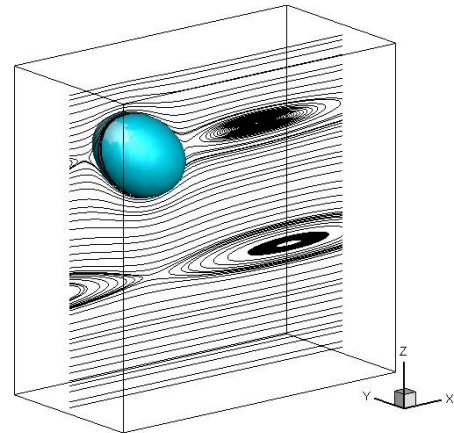


**Figure 13.** Streamlines for the flow with positive pressure gradient

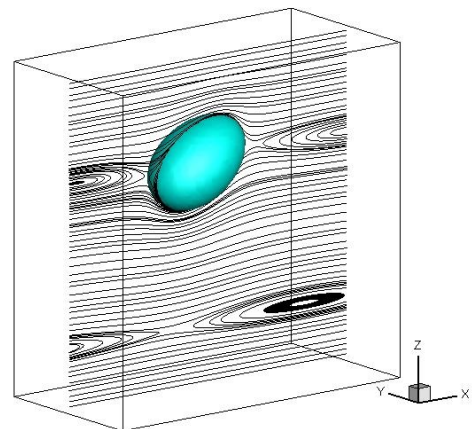


**Figure 14.** Streamlines for the flow with negative pressure gradient

### 3.3. The impact of bubble presence on the shear tension of the wall

In this section, the effect of bubble presence on the shear tension of the channel wall is considered. Shear tension on the upper wall is shown by  $(\tau_{wt})$  and shear tension on the bottom wall is shown by  $(\tau_{wb})$ . No-bubble state of the flow will be calculated with the help of analytical solving. Also in order for making the tensions dimensionless, the quantity of  $\tau_0 = \frac{dp}{dx} \cdot x_l$  has been used. The flow conditions are  $\alpha = \lambda = 0.9$ ,  $Re_d = 10$  and  $\xi = 0.125$ . At first, we will consider the effect of initial position of bubble on the shear tension. If the bubble is released from an initial position located in the bottom half of the channel, in this case greater shear tension will be entered compared to the no-bubble state. As is clear in Fig. 15, bubbles which have been released from the initial position of  $z_0/H = 0.2$  and  $z_0/H = 0.4$ , bear more amount of shear tension on the surface of the bottom wall.

While in the case of the bubbles which have been released from the initial position of  $z_0/H = 0.6$  and  $z_0/H = 0.8$  (Fig. 16), lower shear tension will be entered to the bottom wall compared to the no-bubble state.

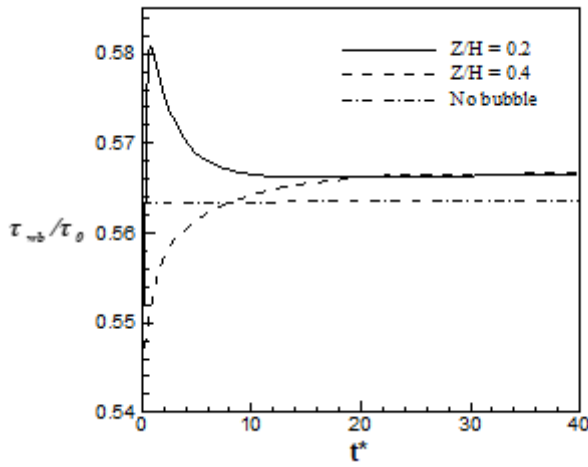


**Figure 15.** Initial position effect of a bubble on shear tension on the bottom wall. The bubble has been released from the initial position of  $z_0/H = 0.4$  and  $z_0/H = 0.2$

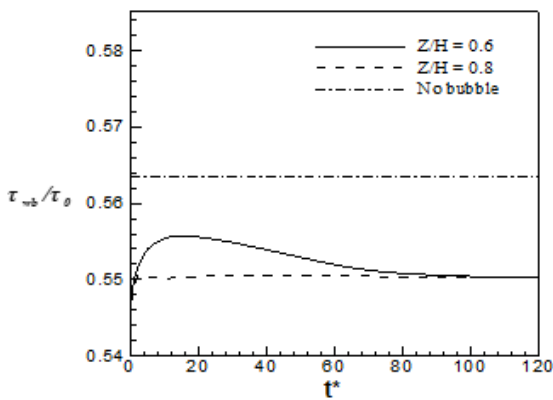


**Figure 16.** Initial position effect of a bubble on shear tension on the bottom wall. The bubble has been released from the initial position of

Now, the conditions of shear tension on the upper wall will be considered. Here, the reverse of the previous conditions is

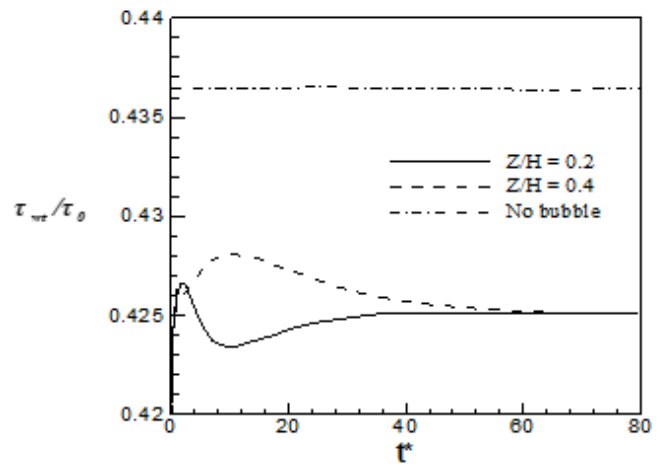
observed. Meaning that bubbles which have been released from the initial position of  $z_0/H = 0.2$  and  $z_0/H = 0.4$ , bear a lower absolute value of shear tension on the upper wall compared to the no-bubble state (Fig. 17).

Fig. 18 indicates the bubbles that have been released from the initial position of  $z_0/H = 0.6$  and  $z_0/H = 0.8$ . As is clear, in this case, shear tension on the upper wall is greater compared to no-bubble state.

Then the effect of bubble's radius or the geometric ratio on the shear tension on the wall will be discussed. The bubble is initially released at  $z_0/H = 0.7$  with relatively large geometric ratios, respectively,  $\xi = 0.18$ ,  $\xi = 0.2$ ,  $\xi = 0.22$ .

Other governing parameters include:  $\alpha = \lambda = 0.8$ ,  $Re_d = 10$  and  $Ca = 0.2$ . The influence of increase of bubble's radius on shear tension on the bottom sheet can be seen in Fig. 19. Shear tension on the bottom sheet decreases with increasing the size of the bubble.

The effect of capillary number on shear tension is shown in Fig. 20. It is clear that the amount of shear tension on the bottom wall decreases with increasing capillary number or decreasing surface tension of bubble.



**Figure 17.** Impact of bubble's initial position on shear tension on the upper wall. Bubble has been released from the initial position of  $z_0/H = 0.2$  and  $z_0/H = 0.4$

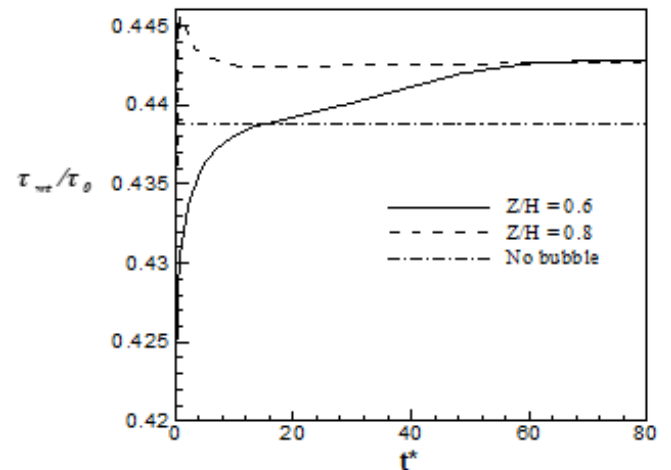


**Figure 18.** Impact of bubble's initial position on shear tension on the upper wall. Bubble has been released from the initial position of  $z_0/H = 0.6$  and  $z_0/H = 0.8$

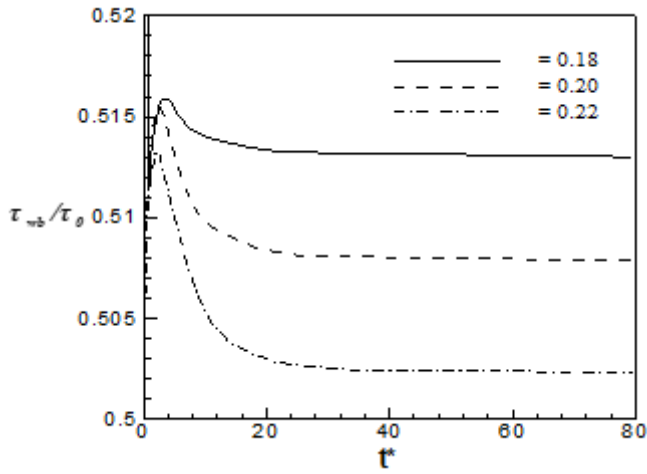


**Figure 19.** Effect of the bubble size on shear tension on the bottom wall

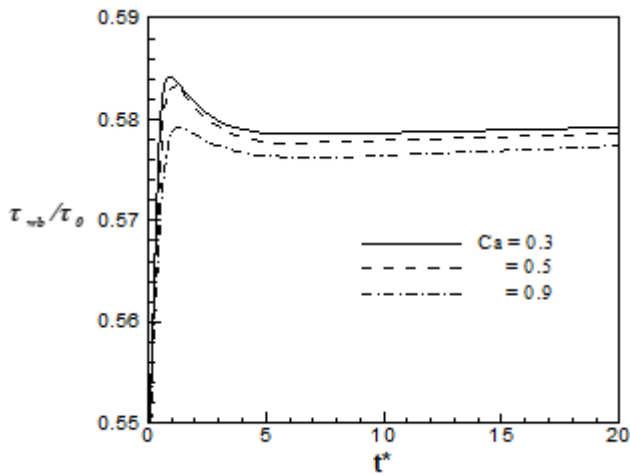


**Figure 20.** Effect of the capillary number on shear tension on the bottom wall

#### 4. CONCLUSIONS

In the present study, three dimensional numerical simulation of lateral migration of a deformable bubble in a compound laminar flow of Couette and Poiseuille in a periodic domain has been studied. The Navier-Stokes equations have been solved using a finite difference/front tracking method. In this method, two sets of grids have been considered. Unsteady incompressible Navier-Stokes equations have been solved with the finite difference method on a staggered regular grid. The interface also has been tracked with one dimension less, explicitly through front tracking method. Based on the obtained predictions it can be concluded that:

1. In the compound flow of Couette and Poiseuille also the Segre Silberberg effect has been observed, but since in the considered flow, the profile of the velocity is not symmetrical to the center line of the channel, the equilibrium position will be slightly different from the simulations performed for only Couette or only Poiseuille flow. As can be seen in the migration curves, the equilibrium distance from the top wall will be  $z_{eq}/H = 0.224$  and from the bottom wall will be  $z_{eq}/H = 0.288$ , which is different from the previous studies.

2. It is observed that with increasing the radius of the bubble, after a transition period, which is associated with a fluctuation, the centroid of the bubble moves away from the upper wall. Because by increase of the bubble's radius, fluid flow is forced to move in a lower distance to the wall and so the lubrication force between the bubble and wall will be increased. This force moves the bubble further away from the wall.

3. Applying a negative pressure gradient will cause the deformation of the bubble to get approximately double and thus the bubble will be in equilibrium state closer to the center line. Because, as a deformable particle is thin, the difference in the velocity of pass flow of the bubble is smaller and thus the force that pushes it toward the wall will be smaller.

4. Flow pattern for both flows with positive and negative pressure gradient is almost identical, and the only difference is in the angle of the main axis of bubble with the wall of the channel.

5. By increase of bubble's radius, shear tension on the bottom wall will be reduced. By increase of capillary number or decrease of surface tension of bubble, the amount of shear tension on the bottom wall will be reduced.

#### REFERENCES

- [1] McCormik ME, Bhattacharyya R. (1973). Drag reduction of a submersible hull by electrolysis. *Naval Engineers Journal* 85: 11-16.
- [2] Esmaeli A, Tryggvason G. (1998). Direct numerical simulations of bubbly flows. Part 1. Low Reynolds number arrays. *Journal of Fluid Mechanics* 377: 313-345.
- [3] Segre G, Silberberg A. (1962). Behavior of macroscopic rigid spheres in Poiseuille flow. Part 1. Determination of local concentration by statistical analysis of particle passages through crossed light beams. *J. Fluid Mech.* 14: 115-135.
- [4] Segre G, Silberberg A. (1962). Behavior of macroscopic rigid spheres in Poiseuille flow. Part 2. Experimental results and interpretation. *J. Fluid Mech.* 14: 136-157.
- [5] Matas JP, Morris JF, Guazzelli E. (2004). Inertial migration of rigid spherical particles in Poiseuille flow. *J. Fluid Mech.* 515: 171.
- [6] Griggs AJ, Zinchenko AZ, Davis RH. (2008). Gravity-driven motion of a deformable drop or bubble near an inclined plane at low Reynolds number. *Int. J. Multiphase Flow* 34: 408-418.
- [7] Li X, Pozrikidis C. (2000). Wall-bounded shear flow and channel flow of suspensions of liquid drops. *Int. J. Multiphase Flow* 26: 1247.
- [8] Nourbakhsh A, Mortazavi S. (2010). A three-dimensional study of the motion of a drop in plane Poiseuille flow at finite Reynolds numbers. *Iranian J Sci Technol Trans B Eng.* 34: 179-196.
- [9] Tsai TM, Miksis MJ. (1994). Dynamics of a drop in a constricted capillary tube. *J. Fluid Mech.* 274: 197-17.
- [10] Mortazavi S, Tafreshi MM. (2013). On the behavior of suspension of drops on an inclined surface. *Physica A* 392: 58-71.
- [11] Bayareh M, Mortazavi S. (2011). Three-dimensional numerical simulation of drops suspended in simple shear flow at finite Reynolds numbers. *International Journal of Multiphase Flow* 37: 1315-1330.

- [12] Bayareh M, Mortazavi S. (2011). Binary collision of drops in simple shear flow at finite Reynolds numbers: Geometry and viscosity ratio effects. *Advances in Engineering Software* 42: 604–611.
- [13] Amiri M, Mortazavi S. (2013). Three-dimensional numerical simulation of sedimenting drops inside a vertical channel. *International Journal of Multiphase Flow* 56: 40–53.
- [14] Mortazavi S, Tryggvason GA. (2011). Numerical study of the motion of drops in Poiseuille flow. Part 1. Lateral migration of one drop. *Journal of Fluid Mechanics* 411: 325-350.
- [15] Unverdi SO, Tryggvason GA. (1992). Front-tracking method for viscous incompressible multi-fluid flows. *J. Comput. Phys.* 100: 25-82.
- [16] Unverdi SO, Tryggvason G. (1992). Computations of multi-fluid flows. *Physics* 60: 70-83.
- [17] Tryggvason G, Bunner B, Esmaeeli A, Juric D, Al-Rawahi N, Tauber W, Jan YJ. (2001). A front tracking method for the computations of multiphase flow. *Journal of Computational Physics.* 169: 708-759.
- [18] Adams J. (1989). Mudpack: Multigrid FORTRAN software for the efficient solution of linear elliptic partial differential equations. *Appl. Math. Comput.* 34: 113-146.
- [19] Feng J, Hu HH, Joseph DD. (1994). Direct simulation of initial value problems for the motion of solid bodies in a Newtonian fluid. Part 1. Sedimentation. *J. Fluid Mech.* 261: 95–134.
- [20] Feng J, Hu HH, Joseph DD. (1994). Direct simulation of initial value problems for the motion of solid bodies in a Newtonian fluid. Part 2. Couette and Poiseuille. *J. Fluid Mech.* 277: 271–301.
- [21] Taylor GI. (1934). The formation of emulsions in definable fields of flow. *Proceedings of the Royal Society of London. Series A, Containing Papers of a Mathematical and Physical Character*, pp. 501-523.
- [22] Schleizer AD, Bonnecaze RT. (1999). Displacement of a two-dimensional immiscible droplet adhering to a wall in shear and pressure-driven flows. *J. Fluid Mech.* 383: 29-54.
- [23] Doddi SK, Bagchi P. (2008). Lateral migration of a capsule in a plane Poiseuille flow in a channel. *Int. J. Multiphase Flow.* 34: 966-986.
- [24] Martinez MJ, Udell KS. (1990). Axisymmetric creeping motion of drops through circular tubes. *J. Fluid Mech.* 210: 565-591.

## NOMENCLATURE

|           |                               |
|-----------|-------------------------------|
| Ca        | Capillary number              |
| d         | Drop diameter (m)             |
| H         | Channel height (m)            |
| p         | Pressure (Pa)                 |
| Re        | Reynolds number               |
| t         | Time (s)                      |
| t*        | Dimensionless time            |
| u         | Velocity field (m/s)          |
| $U_c$     | Channel center velocity (m/s) |
| x         | Eulerian coordinate (m)       |
| $x'$      | Lagrangian coordinate (m)     |
|           | Greek letters                 |
| $\alpha$  | Density ratio                 |
| $\delta$  | Delta Dirac                   |
| $\zeta$   | Dimensionless diameter        |
| $\kappa$  | Curvature                     |
| $\lambda$ | Viscosity ratio               |
| $\mu$     | Viscosity (Pa.s)              |
| $\rho$    | Density (kg/m <sup>3</sup> )  |
| $\sigma$  | Surface tension (N/m)         |